Rip-Current Likelihoods and Predictions on Two Different Bathymetries Observed within 1 Week on the Same Beach in Duck, North Carolina

JUNWOO CHOI[a] AND STEVE ELGAR[b]

[a] *River and Coastal Research Division, Korea Institute of Civil Engineering & Building Technology, Goyang, South Korea*
[b] *Applied Ocean Physics and Engineering Department, Woods Hole Oceanographic Institution, Woods Hole, Massachusetts*

(Manuscript received 8 April 2025, in final form 7 January 2026, accepted 27 January 2026)

ABSTRACT: A rip-current prediction model based on Boussinesq numerical simulations using FUNWAVE (a fully nonlinear Boussinesq wave model) that quantifies rip-current likelihoods is applied to two nearshore bathymetries on the Outer Banks of North Carolina, near the town of Duck. The model is skillful (Brier skill score > 0.5) in reproducing the maximum offshore-directed currents observed with 28 current meters deployed across and along the surfzone for 1 month. During ~1 week within the application period, the observed surfzone bathymetry evolved from relatively alongshore uniform to alongshore inhomogeneous with channels and crescentic sandbars, affecting the likelihood of dangerous rip currents with the same incident wave conditions. Although the maximum difference in rip-current likelihoods between the two bathymetries reached approximately 20%, the hazard indices, predicted by averaging likelihoods from a wide range of observed incident wave conditions, varied by only 6%–7%. The results suggest that at beaches with evolving bathymetry, conservative rip-current warnings should be based on 3D survey data collected during periods of greater alongshore inhomogeneity, when the strongest rip currents are expected.

KEYWORDS: Coastal flows; Currents; Wind waves; Tides; Forecasting; Probability forecasts/models/distribution

1. Introduction

Rip currents pose a significant threat to beachgoers worldwide, causing dozens of deaths each year in the United States and Australia (Gensini and Ashley 2010; NOAA 2022; Surf Life Saving 2022). These currents are understood to form when a strong alongshore variation in wave-induced momentum flux develops (Tang and Dalrymple 1989; Dalrymple et al. 2011) or when alongshore variability in wave-breaking patterns drives vortices (Clark et al. 2012; Feddersen 2014; Peregrine 1998, 1999). Rip currents may develop on any coast where wave breaking is uneven alongshore. There are various types of rip currents, driven by either single dominant factors or complex interactions (Dalrymple et al. 2011; Castelle et al. 2016b), with most being related to offshore or nearshore bathymetry. Transient rip currents, often referred to as "flash rips," also can arise in environments with directional random waves (Peregrine 1998, 1999; Brocchini et al. 2004; Johnson and Pattiaratchi 2006; Kennedy et al. 2006; Clark et al. 2012; Feddersen 2014; Nuss et al. 2025). Rip currents are not limited to open ocean coasts and also can occur along large lake shorelines such as the Great Lakes (Gensini and Ashley 2010; Liu 2020; Liu and Wu 2022).

The prediction of rip currents remains a challenge in ocean forecasting due to the difficulty in predicting both their location and occurrence (Dalrymple et al. 2011; Castelle et al. 2016b). Previous studies have attempted to forecast rip-current occurrences by assessing the risk or probability based on various physical characteristics of a given coastal environment (Lushine 1991; Lascody 1998; Engle 2003; Schrader 2004; Nelko and Dalrymple 2008). An effective rip-current prediction model should incorporate wave characteristics, tidal conditions, and coastal bathymetry and ideally evaluate rip-current dynamics using physics-based formulations. The output should indicate hazard levels through estimates of flow velocity or probability of occurrence. Recently, the U.S. National Oceanic and Atmospheric Administration's National Weather Service (NOAA NWS) developed a statistical forecasting system (Dusek and Seim 2013a,b; Dusek et al. 2014; Churma et al. 2017; Moulton et al. 2017). This system generates empirical relationships using artificial intelligence (AI)-assisted statistical analyses based on lifeguard surveys and incorporates wave height, tidal elevation, wave direction, and a bathymetric event flag as inputs. However, it does not employ a physics-based formulation, with bathymetry only nominally accounted for via a binary event-based adjustment, limiting physical realism. To assess the applicability of such statistical approaches, model outputs were compared with observed rip-current velocities (Moulton et al. 2017), and additional model performance was evaluated using simplified physics-based formulas for rip-current speed (Casper et al. 2024).

A recent approach (Castelle et al. 2025) marks a notable advancement by incorporating a simple physics-based formulation (using wave height, wave period, bar crest elevation, and rip channel depth) and calibrating it with lifeguard-reported hazard levels. Although this method improves representation of local morphology compared with earlier statistical models, it does not include the full complexity of surfzone bathymetry, for which rip-current likelihoods are highly dependent (Choi et al. 2025). To date, no rip-current likelihood forecasting model resolves the three-dimensional structure of coastal bathymetry.

Recently, simulations using FUNWAVE, a phase-resolving Boussinesq model that simulates the vorticities induced by wave-breaking forces (Peregrine 1998; Clark et al. 2012) and includes both persistent and transient rip currents (Chen et al. 1999; Johnson and Pattiaratchi 2006; Geiman and Kirby 2013; Feddersen 2014), have been applied over 3D bathymetry to estimate rip-current hazard indices directly from predicted or

Corresponding author: J. Choi, jwchoi@kict.re.kr

DOI: 10.1175/WAF-D-25-0066.1

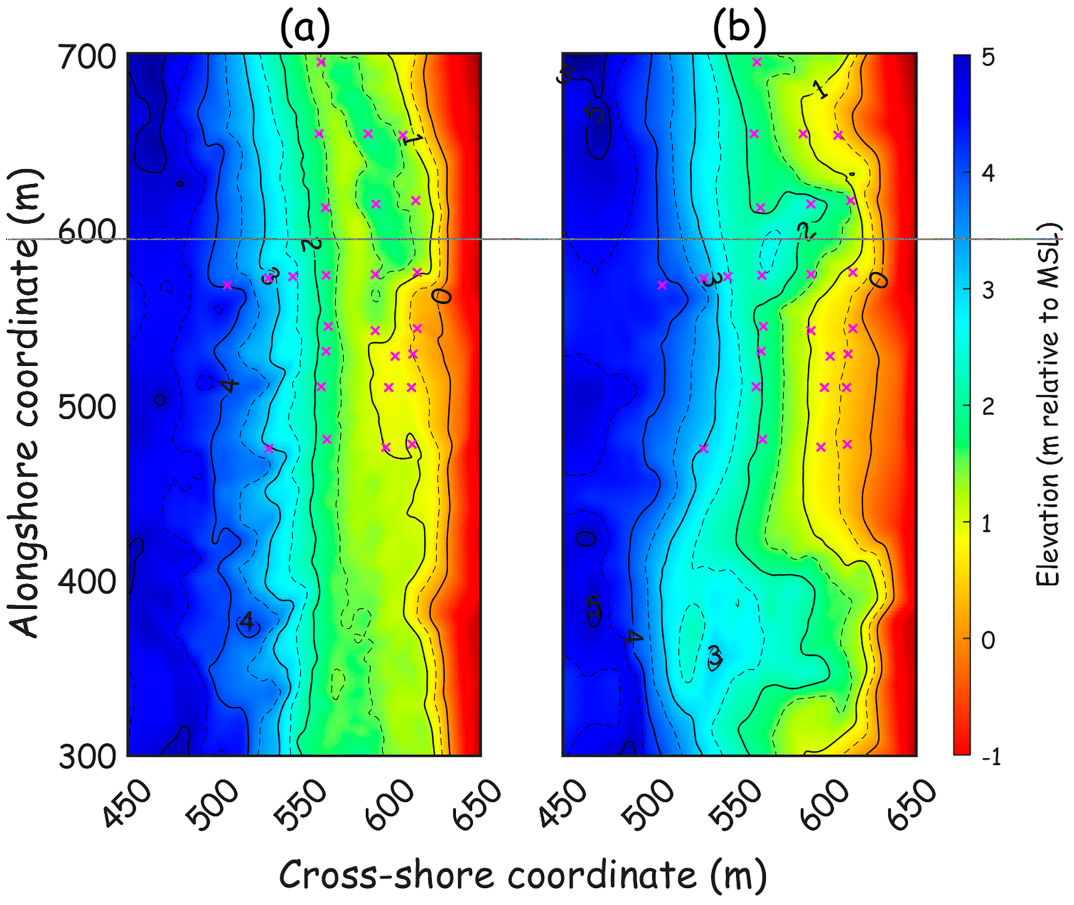

FIG. 1. Color contours of water depth [relative to above mean sea level (MSL); scale on the right, with solid curves every 1 m] as a function of alongshore (y) and cross-shore (x) coordinate surveyed on (a) 25 Sep and (b) 2 Oct 2013 at the U.S. Army Corps of Engineers Field Research Facility in Duck, North Carolina. Magenta cross symbols indicate the locations of current meters.

observed wave and tidal inputs (Choi 2022, 2023, 2025). Coastal areas, each with distinct bathymetries, are expected to show unique distributions of rip-current likelihoods, varying in response to wave height, period, direction, tidal elevation, and frequency and directional spreading.

Here, the presimulation approach (Choi 2025) is applied to investigate rip-current likelihoods on an Atlantic Ocean beach near Duck, North Carolina. The presimulation model is validated by comparisons with in situ observations made with 28 current meters across and along the surfzone for ~1 month. Although the model incorporates observed bathymetry, it does not simulate morphological evolution resulting from changing wave conditions. To assess the impact of such morphological variability, rip-current likelihoods derived from two bathymetric surveys conducted approximately 1 week apart at the same site are compared with each other.

2. Methods

a. Bathymetry

Rip-current likelihoods were investigated for a relatively alongshore uniform surfzone seafloor (depths less than ~3 m, surveyed on 25 September 2013; Fig. 1a) and a more alongshore inhomogeneous surfzone with several channels (depths less than ~3 m, surveyed 1 week later on 2 October 2013; compare yellow and green contours and the 2-m depth curves in Fig. 1b with those in Fig. 1a). Incident waves greater than 2 m high between the surveys caused the morphological evolution, where the variance (σ_y^2) of depths averaged over the range 0.3–2.9-m depth ($525 < x < 610$ m, where x is the cross-shore coordinate) ranged from 0.18 m^2 (σ_y = 0.40 m) on 25 September (Fig. 1a) to 0.36 m^2 (σ_y = 0.60 m) on 2 October (Fig. 1b). These bathymetries were used as the input of the FUNWAVE model.

b. Observations

Wave and tidal data observed from 1 September to 31 October 2013 at Duck were used as inputs to evaluate the performance of the present wave-resolved rip-current likelihood prediction model. Predicted rip-current likelihoods (hazard indices) were compared with observed velocities measured from 26 September to 23 October 2013 (Elgar and Raubenheimer 2020; Elgar et al. 2023) at the same coast. The velocity measurements, obtained from 28 in situ acoustic Doppler velocimeters, were averaged

into 17-s mean currents (approximately two wave periods). From these measurements, a single representative time series was generated from the maximum observed offshore-directed velocity at each time step, assumed to represent the maximum rip-current speed at the study site.

c. Brief description of the FUNWAVE modeling

Here, a phase-resolving, time-evolving wave–current model (FUNWAVE) based on the fully nonlinear Boussinesq framework (Chen et al. 2003) that extends earlier formulations (Wei et al. 1995) and includes a vortex-force representation to capture wave-driven circulation is used. The model also incorporates commonly used physics and numerical options for nearshore applications, including parameterizations for bottom friction, wave breaking, internal-wave generation, and sponge-layer absorption near open boundaries (Chen et al. 1999, 2000; Kennedy et al. 2000). FUNWAVE has been applied widely to nearshore wave transformation and wave–current interaction problems (Chen et al. 1999, 2000; Feddersen 2014, and many others) and also has been used to investigate rip-current dynamics (Johnson and Pattiaratchi 2006; Dalrymple et al. 2011; Geiman and Kirby 2013). Its phase-resolving nature allows the simulation of transient, spatially intermittent rip currents under multidirectional random wave forcing, including the evolution of interference patterns that modulate the forcing in both time and space (Johnson and Pattiaratchi 2006; Spydell and Feddersen 2009; Nuss et al. 2025).

The model setup includes periodic boundaries on the lateral sides, a wavemaker boundary at the offshore deep-water side, and an absorption boundary placed behind the wavemaker to minimize wave reflection. The model domain was based on surveyed bathymetry (1600 m alongshore × 660 m cross-shore), but the domain for analysis was restricted to 1000 m × 600 m to exclude boundary effects. The initial condition begins with still water as a cold start, with a range of incident waves described below. The power spectrum contained 25 bins between 0.07 and 0.22 Hz with varying frequency bandwidth Δf, and the directional spectrum contained 41 bins with varying directional bandwidth $\Delta\theta$. Each bin represents a discrete wave component of constant amplitude at a given frequency and incident angle, with equal energy among components ensured by a constant-volume binning method (Kirby and Özkan 1994; Choi et al. 2015). Although incident wave coherence can affect the simulated patterns of onshore waves (Salatin et al. 2021), that effect is considered small relative to the estimation of the maximum offshore-directed currents and was not considered here, but it should be addressed in future work. The grid sizes in the cross-shore x and alongshore y directions and the computational time step of the simulations for both bathymetries are $\Delta x = 1.5$ m, $\Delta y = 2.0$ m, and $\Delta t = 0.05$ s. Except for the use of a uniform friction coefficient ($f_c = 0.0015$) applied across the domain [rather than the depth-dependent coefficient used by Choi et al. (2015)] to minimize uncertainties associated with tidal variability, all numerical parameters were identical to those used previously. The rip-current velocities were averaged over two incident wave periods from FUNWAVE instantaneous velocity outputs, chosen to approximate the near-instantaneous velocities encountered by swimmers while filtering out wave-orbital velocities. The results were insensitive to the choice of a longer averaging period (Choi et al. 2025). Model output (surface displacement, wave height, vorticity, and current vectors) was documented previously (Choi et al. 2025).

d. Scenarios for rip-current simulations

To characterize how rip-current likelihood varies with incident conditions and the two observed bathymetries, ensembles of numerical simulations spanning significant wave height H, mean wave period T, tidal elevation E, mean wave direction θ, frequency-spectrum spreading F, and directional spreading D were run. The frequency-spreading parameter F is (Goda 1970)

$$F = \frac{2}{m_0^2}\int_0^\infty f\, S_f^2 df, \tag{1}$$

where f denotes frequency, S_f is the imposed one-dimensional frequency spectrum, and the spectral moments are $m_n = \int_0^\infty f^n S_f df$. The directional-spreading parameter D is defined as (Longuet-Higgins et al. 1963)

$$D = \sqrt{dm_2/dm_0}, \tag{2}$$

where $dm_n = \int_0^\infty \int_0^{2\pi} \theta^n S d\theta df$, θ is the direction, and S is the input frequency–directional spectrum. In the simulations, the input spectra were specified using the Joint North Sea Wave Project (JONSWAP) peak-enhancement factor γ and the Mitsuyasu-type directional parameter σ_θ (Mitsuyasu et al. 1975). For consistency with the analysis metrics, γ and σ_θ were mapped to the corresponding spreading measures F and D defined in Eqs. (1) and (2).

The simulations produce the rip-current likelihood distributions as functions of wave height and period (H, T), wave height and direction (H, θ), wave height and tidal elevation (H, E), wave height and frequency spectral spreading (H, F), and wave height and direction spectral spreading (H, D). Significant wave height was used as a primary parameter because wave height and subsequent breaking are the most critical factors for rip-current generation. Six wave–height conditions were considered, producing 36, 60, 42, 30, and 42 scenarios for (H, T), (H, θ), (H, E), (H, F), and (H, D), respectively, yielding a total of 210 simulation cases for each of the two bathymetries. The detailed boundary conditions are provided in appendix A (Table A1). Representative values for the parameters were chosen to produce strong rip currents, including 0-m tidal elevation, normal 0° direction, narrow spectrum ($F = 6$, $D = 20$), and 9-s wave period. The simulations required approximately 37 days on a single-node configuration using six PCs (96 cores) equipped with Intel i7 CPUs and 32 GB of RAM (each case took less than 20 days to run on a single core).

e. Quantification of rip-current likelihood

Rip-current likelihood was quantified for each coastal scenario using the following procedure. From each simulation, a time series of the domainwide maximum offshore-directed

velocity, $v_{\text{maxrip}}(t)$, was extracted. This time series summarizes the strongest instantaneous seaward-directed jet that occurs anywhere in the computational domain at each time step and thus provides a measure of episodic rip-current intensification. Most of the maximum velocities occur in the surfzone and close to or within bathymetric channels (appendix B, Fig. B1). For a given pair of forcing or environmental bins i and j, the likelihood f_{ij}(%) was defined as the fraction of the simulation time during which v_{maxrip} exceeds a prescribed "danger" threshold, v_{danger}. Rather than adopting a single threshold, this exceedance fraction was computed for a small set of thresholds, and the resulting percentages were averaged (Choi et al. 2025):

$$f_{ij} = \frac{1}{N}\left(\frac{t_{v_{\text{maxrip}}>v_{\text{danger\_1}}}}{t_{\text{simulation}}} + \frac{t_{v_{\text{maxrip}}>v_{\text{danger\_2}}}}{t_{\text{simulation}}} + \cdots + \frac{t_{v_{\text{maxrip}}>v_{\text{danger\_}N}}}{t_{\text{simulation}}}\right). \tag{3}$$

Here, $t_{v_{\text{maxrip}}>v_{\text{danger}}}$ is the total duration for which the maximum offshore-directed velocity exceeds the chosen threshold and $t_{\text{simulation}}$ is the full simulation length. The thresholds were set to v_{danger} = 0.5, 0.75, 1.0, 1.25, and 1.5 m s^{-1} (i.e., $v_{\text{danger\_1}}$, $v_{\text{danger\_2}}$, …, $v_{\text{danger\_}N}$). Using multiple thresholds acknowledges that danger in the surfzone is not associated with a single universal speed but depends strongly on swimmer capability (age, fitness, flotation, and surf conditions). For context, elite swimmers can approach ~1 m s^{-1} in still water, whereas professional lifeguards typically achieve ~0.7–0.9 m s^{-1} in surf conditions (Tipton et al. 2008), and observed bather speeds within rip currents are often ~0.2–0.4 m s^{-1} (Yuan et al. 2023). In addition, hazard ratings used in studies of bather escape strategies combine flow speed and depth (McCarroll et al. 2015; Castelle et al. 2016a), drawing on human-stability criteria developed for floodwaters (RESCDAM 2000; HR Wallingford 2005), where a representative threshold of ~0.5 m s^{-1} commonly is used. A sensitivity analysis of the likelihood metric to threshold selection is provided elsewhere (Choi et al. 2025).

f. A function of rip-current likelihoods

The numerically simulated likelihoods [Eq. (3)] are presented by the five two-dimensional distributions $f_{HT}(H, T)$, $f_{H\theta}(H, \theta)$, $f_{HE}(H, E)$, $f_{HF}(H, F)$, and $f_{HD}(H, D)$. The predicted likelihood, based on wave and tidal data (i.e., H_1, T_1, θ_1, E_1, F_1, D_1) observed or forecasted at a given time near the coast, can be obtained by the rip-current hazard index R, which is expressed as the average of the five likelihoods:

$$R = [f_{HT}(H_1, T_1) + f_{H\theta}(H_1, \theta_1) + f_{HE}(H_1, E_1) + f_{HF}(H_1, F_1) + f_{HD}(H_1, D_1)]/5. \tag{4}$$

The rip-current hazard index has been defined as (Choi 2025)

$$R(H, T, E, \theta, F, D) = \alpha_w(\beta_T f_{HT} + \beta_E f_{HE} + \beta_\theta f_{H\theta} + \beta_F f_{HF} + \beta_D f_{HD}), \tag{5}$$

where β_T, β_E, β_θ, β_F, and β_D are empirical weighting coefficients and α_w is a safety factor to account for additional uncertainties, including seasonal variations in incident wave conditions and short-term local surfzone variability. Here, the empirical coefficients are set as β_T = 0.2, β_E = 0.2, β_θ = 0.2, β_F = 0.2, and β_D = 0.2, and the safety factor α_w = 1.0. Although these coefficients were derived from video monitoring and surveys, sensitivity tests indicated minimal influence (Choi 2025), and therefore, mean values were used here.

Additionally, to assess the simplified approximation in Eq. (4), hazard indices were computed using a machine learning algorithm in MATLAB. Ideally, these indices should be derived from a six-dimensional likelihood function $f_{H,T,E,\theta,F,D}$ based on a more extensive set of simulations rather than relying on five separate two-dimensional likelihoods. To approximate this, a shallow neural network employing Bayesian regularization backpropagation (*trainbr* routine; MathWorks 2024) was used to generate a six-dimensional AI-based likelihood ($f'_{H,T,E,\theta,F,D}$). The network, consisting of a single hidden layer, was trained using the five numerically simulated likelihood distributions $f_{HT}(H, T)$, $f_{H\theta}(H, \theta)$, $f_{HE}(H, E)$, $f_{HF}(H, F)$, and $f_{HD}(H, D)$, effectively interpolating the relationships among these distributions.

3. Results

a. Rip-current likelihoods on the 2 October bathymetry

The rip-current likelihood distributions were derived for varying conditions for each of the two bathymetries (2 October distributions are shown in Fig. 2). To facilitate graphical representation and enhance the functionality of the prediction model, likelihoods were set to 0% at 0-m wave height and 100% at 3.0-m wave height across all parameter ranges, including direction, elevation, and spectral spreading. Intermediate values between scenarios were interpolated. Each likelihood also was normalized by the maximum percentile among all five distributions. Due to computational constraints, five two-dimensional distributions were used instead of a single six-dimensional distribution.

The resulting likelihood distributions [wave height vs period, $f_{HT}(H, T)$; wave height vs wave direction, $f_{H\theta}(H, \theta)$; wave height vs tidal elevation, $f_{HE}(H, E)$; wave height vs frequency spectral spreading, $f_{HF}(H, F)$; and wave height vs directional spectral spreading, $f_{HD}(H, D)$] illustrate how rip-current activity depends on incident wave height, wave period, tidal elevation, and spectral properties (Fig. 2). Rip-current likelihood generally increased with wave height and reached a maximum at wave periods of about 10–11 s. This maximum is possibly caused by a resonance effect between incident-wave variability and alongshore morphological variability, although further investigation is required (Choi et al. 2025). Normally incident waves generate converging feeder currents, whereas oblique waves predominantly drive alongshore currents, consistent with prior studies (Dalrymple et al. 2011; Castelle et al. 2016b; Moulton et al. 2017; and many others). Lower tidal elevations corresponded to increased likelihoods, likely due to the widened surfzone at lower water levels. Additionally, narrower frequency spectra and broader directional spectra were associated with enhanced rip-current likelihood.

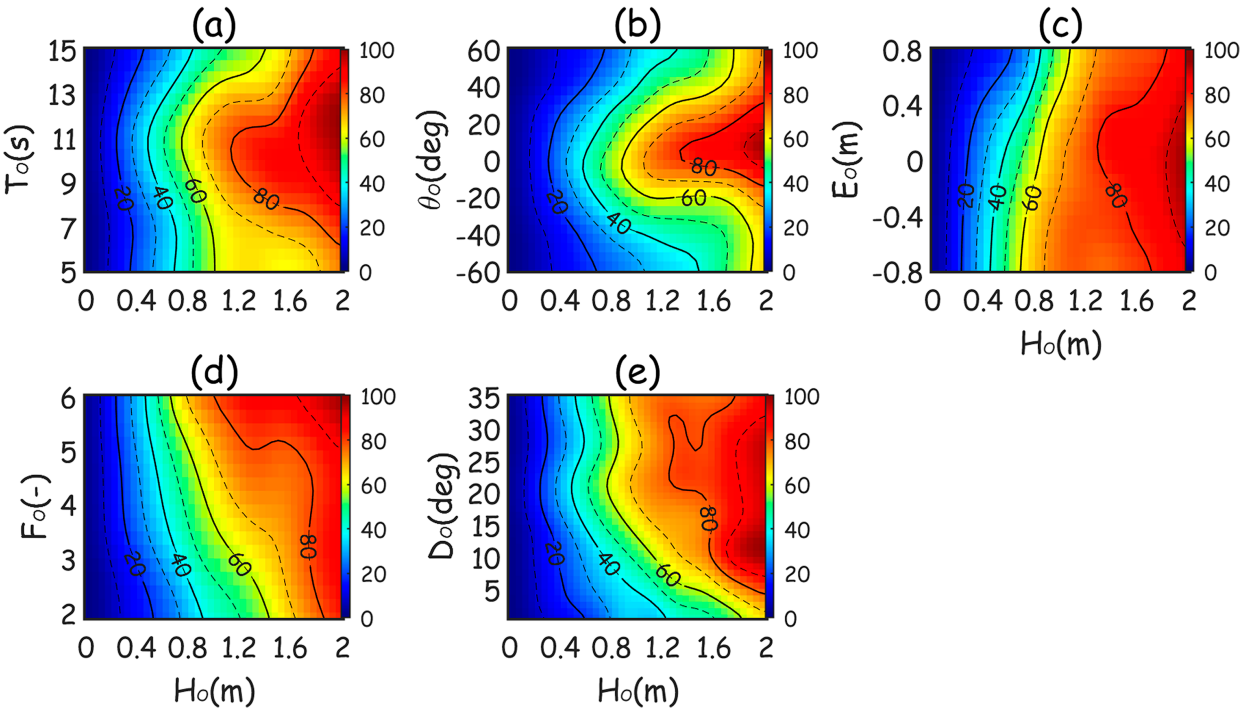

FIG. 2. Color contours (scales on the right) of rip-current likelihoods as a function of (a) wave height and period f_{HT} (%) with $\theta = 0°$, $E = 0$ m, $F = 6$, and $D = 21°$ ($\gamma = 9.9$ and $\sigma_\theta = 20°$); (b) wave height and direction $f_{H\theta}$ (%) with $T = 9$ s, $E = 0$ m, $F = 6$, and $D = 21°$ ($\gamma = 9.9$ and $\sigma_\theta = 20°$); (c) wave height and tidal elevation f_{HE} (%) with $T = 9$ s, $\theta = 0°$, $F = 6$, and $D = 21°$ ($\gamma = 9.9$ and $\sigma_\theta = 20°$); (d) wave height and spectral width f_{HF} (%) with $T = 9$ s, $\theta = 0°$, $E = 0$ m, and $D = 21°$ ($\sigma_\theta = 20°$); and (e) wave height and directional spectral spread f_{HD} (%) with $T = 9$ s, $\theta = 0°$, $E = 0$ m, and $F = 6$ ($\gamma = 9.9$) for the 2 Oct bathymetry.

b. *Validation of prediction model*

To validate the prediction model, the rip-current hazard indices, derived from the approximation of Eq. (4) using the likelihood database (Fig. 2), were compared with rip-current velocities observed at 28 locations during the same period at Duck (Elgar and Raubenheimer 2020; Elgar et al. 2023). Observations were summarized by selecting the maximum offshore-directed velocity from these locations at each time step to represent the maximum rip-current speed. The patterns of the maximum observed offshore-directed currents resemble those of the hazard indices predicted using the numerical model [cf. the black curve (observations) with the red curve (predictions) in Fig. 3a].

The performance of the model in predicting the rip-current hazard index was evaluated using several statistical metrics, including reliability diagrams, Brier skill score (BSS), accuracy (ACC), probability of detection (POD), false alarm ratio (FAR), false positive rate (FPR), and Youden's index. Detailed descriptions of the statistical assessment methods and corresponding results are provided in appendix C. Reliability analysis indicated that for a threshold speed of 0.65 m s^{-1}, the model aligned most closely with the ideal 1:1 relationship, overpredicting events below 0.4 and underpredicting above 0.6 m s^{-1} (Fig. C1). The model showed its highest overall skill (BSS $\approx$ 0.5–0.6) for threshold speeds between 0.55 and 0.75 m s^{-1} (Fig. C2). Notably, the model demonstrated robust predictive capability, maintaining accuracy values greater than 0.9 for threshold speeds of 0.55–0.65 m s^{-1} and critical likelihoods of 0.4–0.6 m s^{-1}.

For example, at a threshold speed of 0.55 m s^{-1} and a critical likelihood of 0.4, the model achieved ACC and POD values of 0.92, with an FAR of 0.03, an FPR of 0.07, and a Youden's index of 0.85 (Table C1). At this setting, the Brier skill score exceeded 0.5, and the area under the receiver operating characteristic (ROC) curve (AUC) was 0.97 (Fig. C2). These results indicate that, when applied operationally, a rip-current forecast system using a 40% critical likelihood for rip-current speeds above 0.55 m s^{-1} can deliver accuracy exceeding 90% while retaining strong discriminatory power (Youden's index $\approx$ 0.85).

However, the bathymetry surveyed on 2 October was used, and visual observations suggest it changed during a storm on 9 October (incident significant wave heights were greater than 3 m; Fig. 3c), possibly explaining the difference between the observed currents and the simulated hazard indices after this time. In addition, the 28 spatially separated gauges may not always observe the maximum rip-current velocity across the entire surfzone (see appendix B, Fig. B1). The effect of bathymetric evolution during the application period was therefore examined by comparing likelihoods derived from the 25 September survey with those from the 2 October survey.

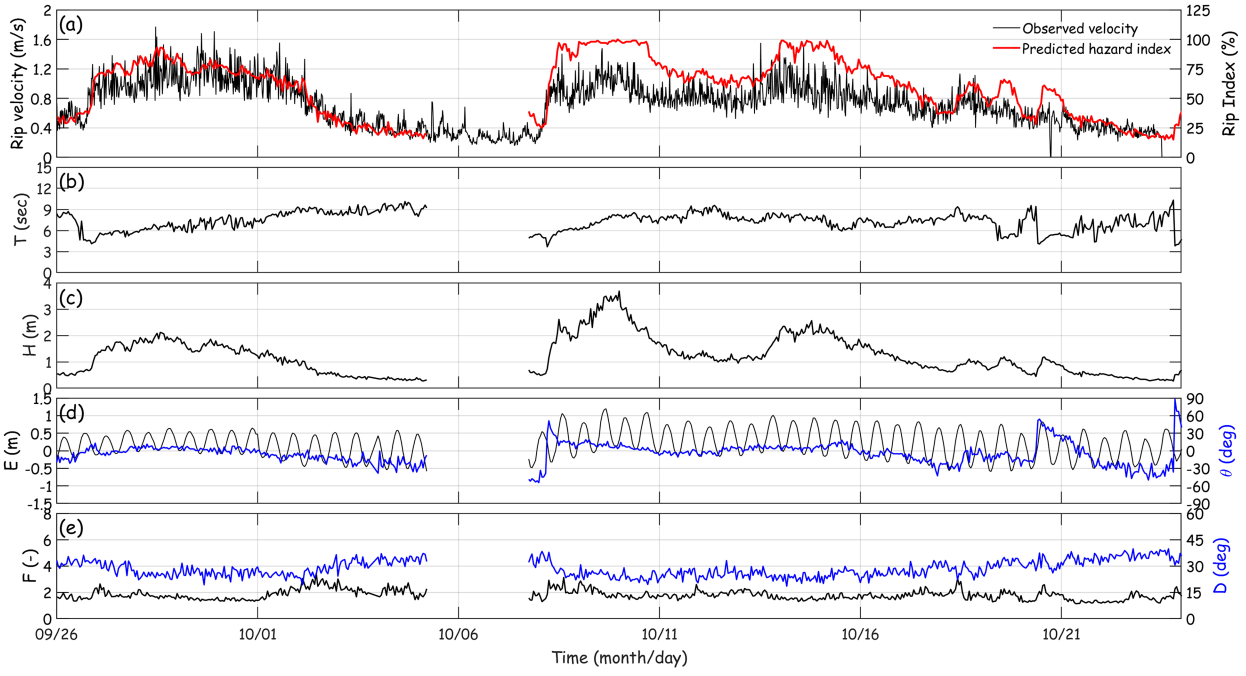

FIG. 3. (a) Observed maximum offshore-directed velocity (black curve; left axis) and predicted hazard index (%) based on the 2 Oct bathymetry (red curve; right axis), and observed (b) averaged wave period, (c) significant wave height, (d) tidal elevation (black curve; left axis) and wave direction (blue curve; right axis), and (e) spreading of frequency spectrum (black curve; left axis) and spreading of directional spectrum (blue curve; right axis) vs time (month/day) in September–October. The observed maximum offshore-directed rip-current velocity is based on the average over two wave periods.

c. *Comparison between likelihoods on two different bathymetries on the same beach*

The rip-current likelihood distributions derived from varying wave and tidal conditions show the behavior of rip currents influenced by changes in surfzone bathymetries. Rip-current likelihoods vary with wave height and wave period (Fig. 4). In both bathymetries, the likelihoods increase with wave height and peak at wave periods of approximately 10–11 s. The distribution patterns are similar; however, the likelihoods for the October bathymetry are higher, especially for wave heights around 0.8 m with periods ranging from 9 to 15 s, likely owing to the stronger gradient of breaking forces caused by the more alongshore-inhomogeneous bathymetry in breaking depths.

Likelihoods generally increase with wave height and as waves propagate more perpendicularly to the shoreline for both bathymetries (Fig. 5). The October bathymetry (Fig. 1b)

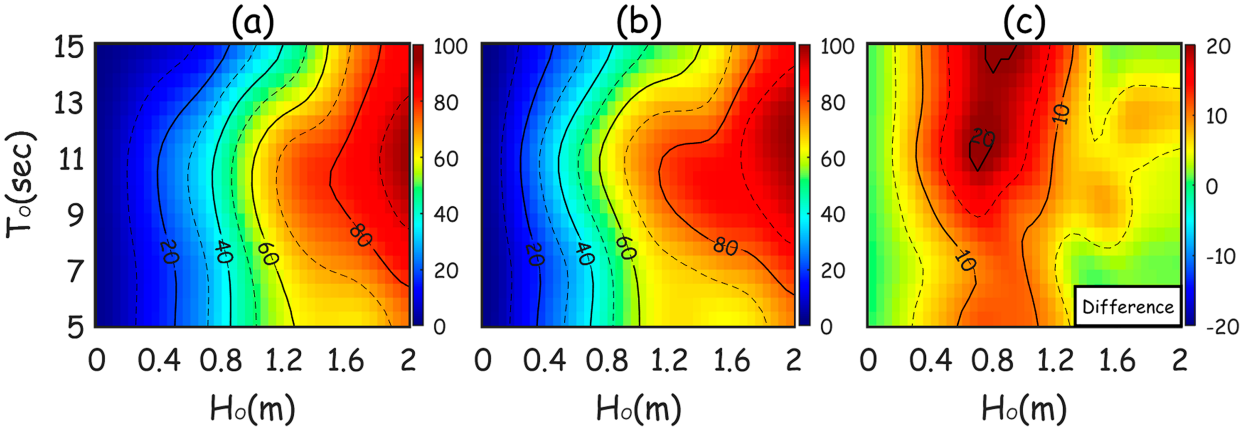

FIG. 4. Color contours (scales on the right) of rip-current likelihood as a function of wave height and period f_{HT} (%) for the bathymetries observed in (a) September and (b) October with $\theta = 0°$, $E = 0$ m, $F = 6$, and $D = 21°$ ($\gamma = 9.9$ and $\sigma_\theta = 20°$); (c) their difference ($f_{HT,\text{October}} - f_{HT,\text{September}}$).

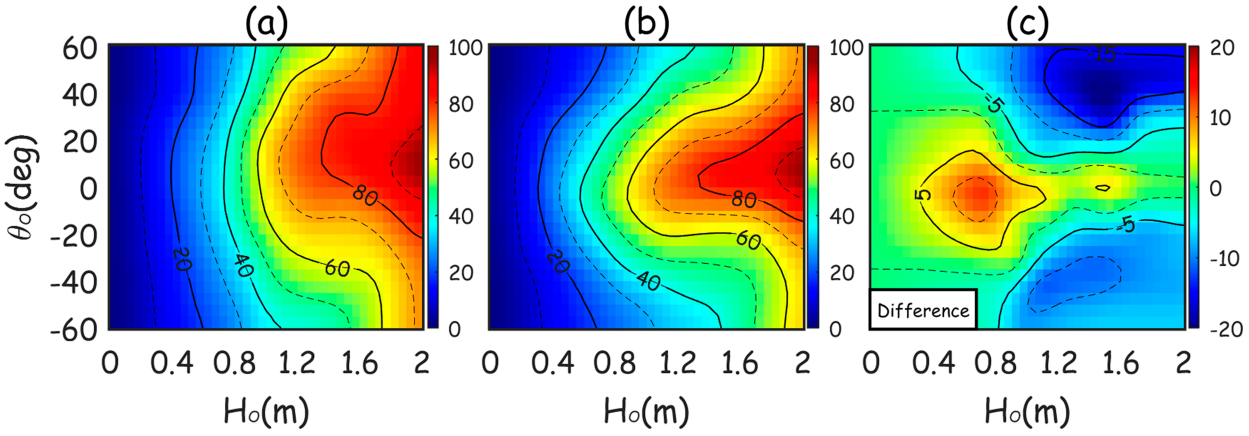

FIG. 5. Color contours (scales on the right) of rip-current likelihood as a function of wave height and direction $f_{H\theta}$ (%) for the bathymetries observed in (a) September and (b) October with $T = 9$ s, $E = 0$ m, $F = 6$, and $D = 21°$ ($\gamma = 9.9$ and $\sigma_\theta = 20°$); (c) their difference ($f_{H\theta,\text{October}} - f_{H\theta,\text{September}}$).

has higher likelihoods for normally incident 0.8 m waves, whereas the September bathymetry (Fig. 1a) has higher likelihoods for larger oblique waves, possibly due to stronger shear fluctuations (Feddersen 2014; Castelle et al. 2016b).

Lower tidal levels tend to correspond with higher likelihoods, likely owing to the expanded surfzone over the gentler cross-shore slope during low tide for both bathymetries (Fig. 6). The biggest difference in likelihoods occurs during higher tides for 0.6–0.8-m wave heights (Fig. 6c), likely because in the October bathymetry, alongshore inhomogeneity is more pronounced at the depths where these waves break during high tide ($E = 0.3$ m).

Likelihoods are higher for narrower frequency spectra (Fig. 7), as steeper wave-breaking profiles dominate in such conditions for both bathymetries. Likelihoods are bigger for the October bathymetry (Fig. 1b) than for the smoother September bathymetry (Fig. 1a) for a range of spectral widths and wave heights (Fig. 7c).

Likelihoods increase with broader directional spectra, which are known to favor the formation of transient rip currents (Spydell and Feddersen 2009; Suanda and Feddersen 2015; Moulton et al. 2023) (Figs. 8a,b), with higher likelihoods on the October bathymetry than the smoother September bathymetry, especially for incident wave heights of ~0.8 m (Fig. 8c).

Overall, the analysis reveals up to a 20% difference in rip-current likelihoods between the two bathymetries, surveyed ~1 week apart for identical wave and tidal conditions, underscoring the significant impact of surfzone changes on rip-current prediction.

d. *Performance of prediction model derived from two bathymetries*

Hazard indices derived from the approximation of Eq. (4) are compared with those estimated using a shallow neural network trained on rip-current likelihoods from the September and October bathymetries (Fig. 9). Similar to the simulations, when either Eq. (4) or the AI model is driven with the observed incident wave conditions (Figs. 9b–e), the likelihoods (hazard indices) using the alongshore inhomogeneous October bathymetry

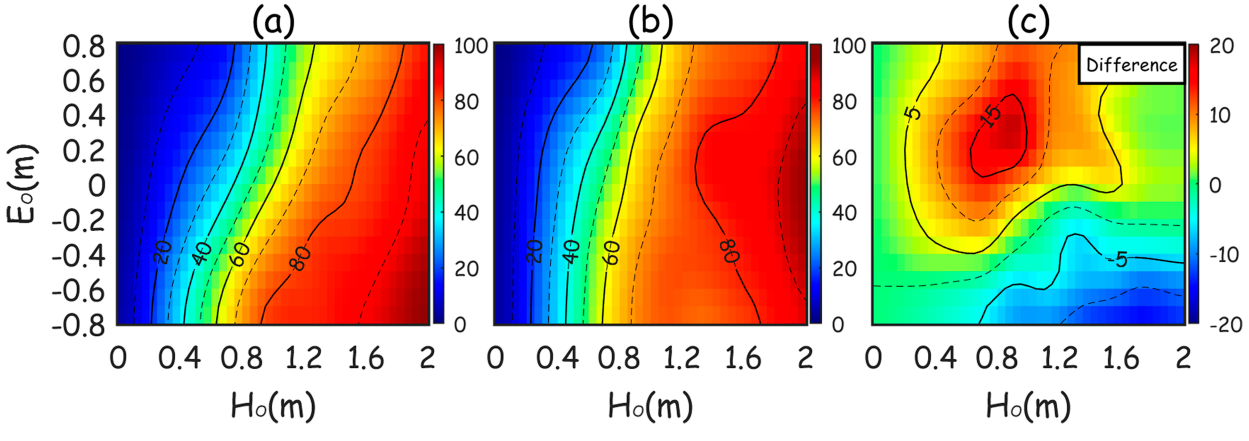

FIG. 6. Color contours (scales on the right) of rip-current likelihood as a function of wave height and tidal elevation f_{HE} (%) for the bathymetries observed in (a) September and (b) October with $T = 9$ s, $\theta = 0°$, $F = 6$, and $D = 21°$ ($\gamma = 9.9$ and $\sigma_\theta = 20°$); (c) their difference ($f_{HE,\text{October}} - f_{HE,\text{September}}$).

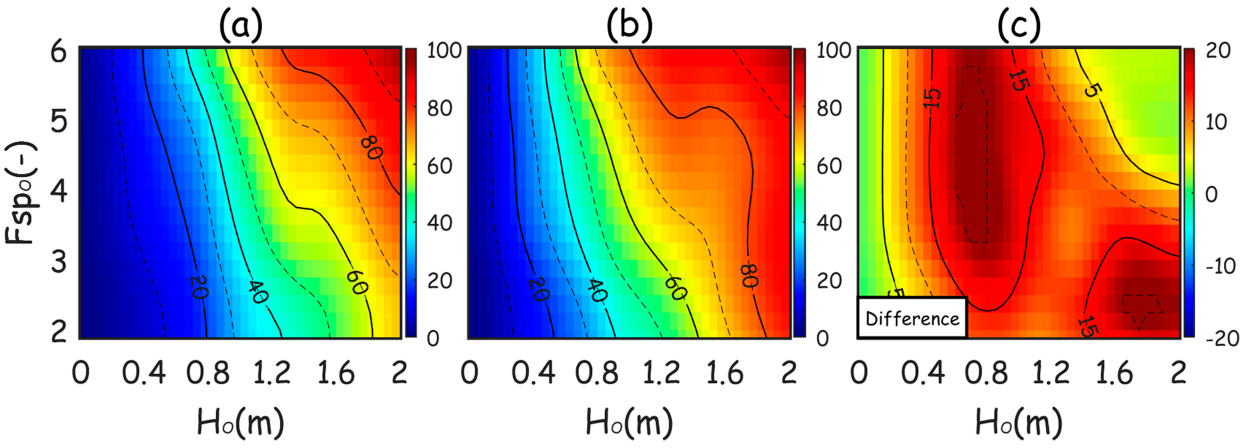

FIG. 7. Color contours (scales on the right) of rip-current likelihood as a function of wave height and spectral width f_{HF} (%) for the bathymetries observed in (a) September and (b) October with $T = 9$ s, $\theta = 0°$, $E = 0$ m, and $D = 21°$ ($\sigma_\theta = 20°$); (c) their difference ($f_{HF,\text{October}} - f_{HF,\text{September}}$).

are higher than those using the smoother September bathymetry (cf. red with black curves, and blue with magenta curves in Fig. 7a). However, the differences due to bathymetric variations (root-mean-square difference ~7%) are smaller than the discrepancies between Eq. (4) and the AI-based estimates (12%–14%), indicating that the choice of bathymetry has a smaller impact than the choice of approximation method. Thus, despite differences in bathymetry, the overall rip index estimates remain relatively consistent. Although bathymetric changes influence rip-current likelihood predictions, the resulting variations in predicted rip indices are relatively limited. Therefore, utilizing the bathymetry that produces higher rip-current likelihoods as a reference offers a conservative and reliable approach for safety forecasting.

Following the approach described previously (Choi 2025), the likelihoods from the FUNWAVE simulations were normalized by their maximum values to compile each distribution for the database, producing relatively large index values in Eq. (4). In contrast, the AI-based approach estimates a six-dimensional likelihood function from the trained model and uses the simulation-derived values directly. The AI-based approach is a practical alternative to running computationally expensive simulations for all scenarios, although operational use may require adjustments such as safety factors or post-event parameterizations (Moulton et al. 2017).

4. Summary

A rip-current prediction and warning model that quantifies the likelihood of rip-current occurrence was applied to two bathymetries observed near Duck, North Carolina. The rip-current likelihoods (hazard indices) predicted by the model are similar to the maximum offshore-directed currents observed over a month. Model validation demonstrated strong

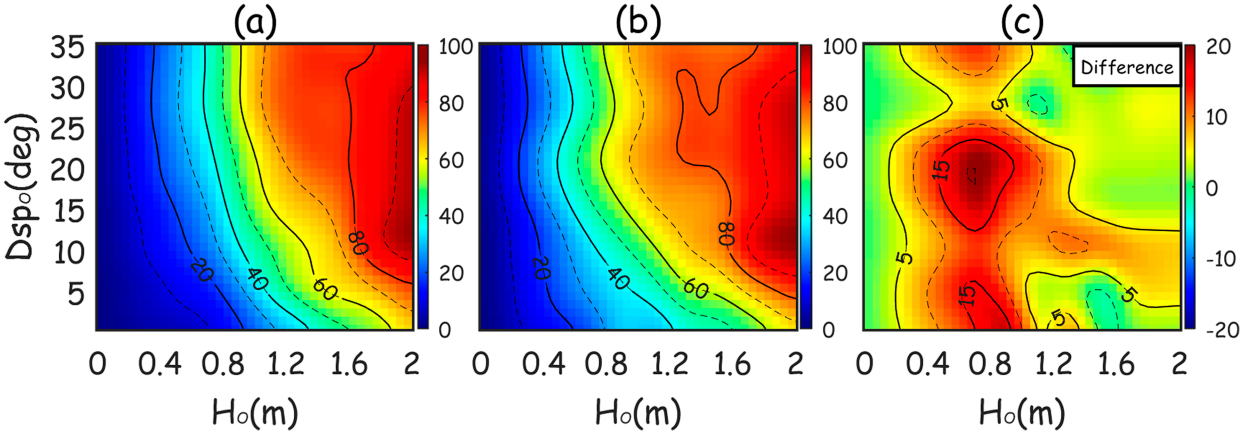

FIG. 8. Color contours (scales on the right) of rip-current likelihood as a function of wave height and directional spectral spread f_{HD} (%) for the bathymetries observed in (a) September and (b) October with $T = 9$ s, $\theta = 0°$, $E = 0$ m, and $F = 6$ ($\gamma = 9.9$); (c) their difference ($f_{HD,\text{October}} - f_{HD,\text{September}}$).

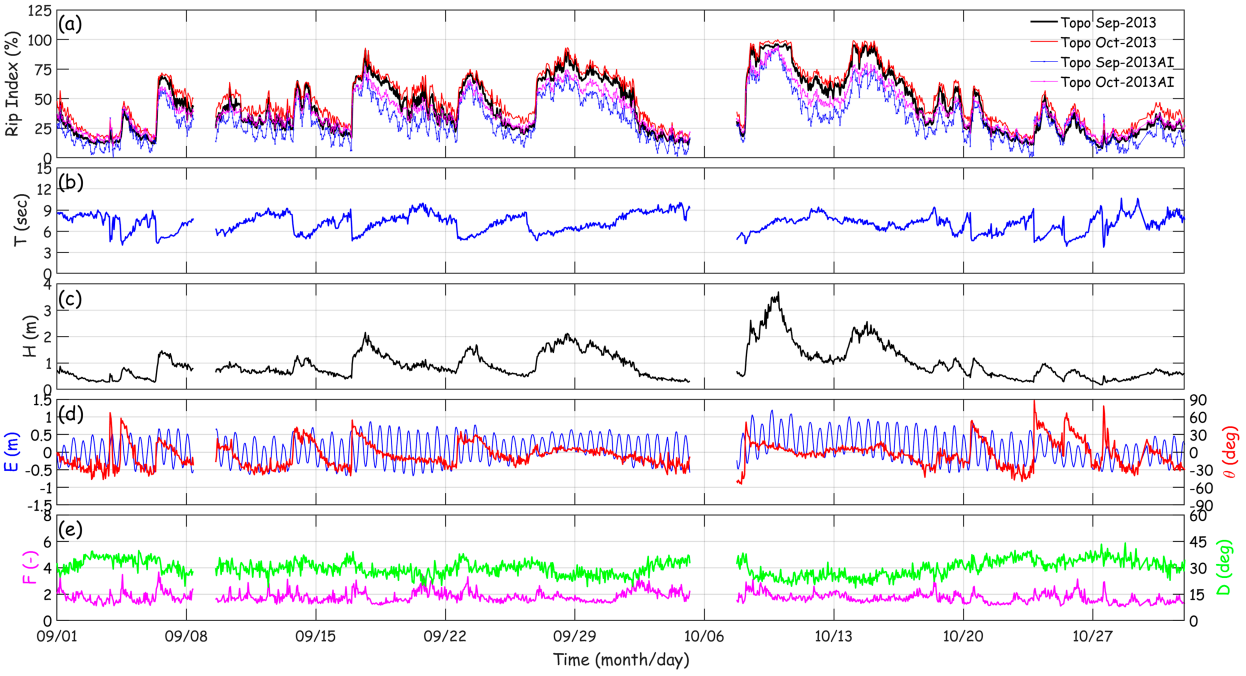

FIG. 9. (a) Rip-current likelihood index and observed (b) averaged wave period, (c) significant wave height, (d) tidal elevation (blue curve; left axis) and wave direction (red curve; right axis), and (e) spreading of frequency spectrum (magenta curve; left axis) and spreading of directional spectrum green curve; right axis) vs time (month/day) in September and October 2013. In (a), the black curve is the hazard index using Eq. (4) on the September bathymetry, the red curve is the hazard index using Eq. (4) on the October bathymetry, and the blue and magenta curves are the indices estimated with the machine learning results of the September and October bathymetries, respectively.

predictive skill, with accuracy above 90%, Youden's index near 0.85, and Brier skill score values exceeding 0.5 at a threshold speed of 0.55 m s^{-1}, confirming its effectiveness for rip-current hazard forecasting. Comparisons highlighted the critical role of accounting for bathymetric changes in operational applications.

Rip-current likelihoods were higher on the more inhomogeneous bathymetry than on the more alongshore uniform surfzone seafloor, especially for incident wave heights around 0.8 m, shore normal waves, high tide levels, and broader frequency spectra. In contrast, the likelihoods for the smoother bathymetry were higher than those for the inhomogeneous seafloor when waves were more oblique and during lower tides. However, when observed wave and tidal inputs were considered, the differences in the predicted rip-current likelihoods (hazard indices) derived using the two bathymetries were, on average, less than ~7%. An alternative approach using AI produced similar results, with slightly higher differences in the rip indices on the two bathymetries. Given the safety concerns that necessitate predictions for a worst-case scenario, a bathymetry (either from historical observations or assumed potential "worst case" bathymetry) that provides the highest likelihood of dangerous rip currents should be used, especially when considering the cost of updating the prediction model with new bathymetry.

Acknowledgments. We thank the Field Research Facility and PVLAB field crews for performing bathymetric surveys and for deploying, maintaining, and recovering in situ sensors in difficult surfzone conditions. Funding was provided by the Korea Hydrographic and Oceanographic Agency and Geosystem Research Corp. of South Korea, the U.S. National Science Foundation, and a National Security Science and Engineering Faculty Fellowship from the Office of the U.S. Secretary of Defense.

Data Availability Statement. The oceanographic observations and beach survey data used in this study are publicly available from the USACE ERDC Field Research Facility data catalog (https://chldata.erdc.dren.mil/thredds/catalog/frf/catalog.html). The RODSEX velocity dataset (Ring Of Doom Experiment: Vorticity and Advection in the Surf Zone) is available from the PV Lab website (https://pv-lab.org/rodsex/). Numerical simulations were performed using FUNWAVE, developed by the Center for Applied Coastal Research at the University of Delaware, and documentation is available online (https://www1.udel.edu/kirby/programs/funwave/funwave.html). Machine learning analyses used shallow neural network tools in the MATLAB R2024b Deep Learning Toolbox (https://www.mathworks.com/products/deep-learning.html).

TABLE A1. Wave and tidal conditions used as inputs to the FUNWAVE simulations of random wave–driven rip currents at Duck, North Carolina, based on the observed bathymetry. Elevation is referenced to MSL, and $\theta = 0°$ denotes normally incident waves. Parentheses for the 9-s cases indicate the number of simulations associated with each parameter [reproduced from Choi et al. (2025), published under a CC BY license].

	T (s)						
H (m)	5	7	9		11	13	15
0.7	$\theta = 0°$, $E = 0$ m, $F = 6.0$, $s = 21°$	$\theta = 0°$, $E = 0$ m, $F = 6.0$, $D = 21°$	$E = 0$ m, $D = 21°$, $F = 6.0$, $-40 \le \theta \le 40°$ (10) $\theta = 0°$, $D = 21°$, $F = 6.0$, $-0.8 \le E \le 0.8$ m (7)	$\theta = 0°$, $E = 0$ m, $D = 21°$, $2 \le F \le 6$ (5) $\theta = 0°$, $E = 0$ m, $F = 6$, $0° \le D \le 35°$(7)	$\theta = 0°$, $E = 0$ m, $F = 6.0$, $D = 21°$	$\theta = 0°$, $E = 0$ m, $F = 6.0$, $D = 21°$	$\theta = 0°$, $E = 0$ m, $F = 6.0$, $D = 21°$
0.9	$\theta = 0°$, $E = 0$ m, $F = 6.0$, $D = 21°$	$\theta = 0°$, $E = 0$ m, $F = 6.0$, $D = 21°$	$E = 0$ m, $D = 21°$, $F = 6.0$, $-40 \le \theta \le 40°$ (10) $\theta = 0°$, $D = 21°$, $F = 6.0$, $-0.8 \le E \le 0.8$ m (7)	$\theta = 0°$, $E = 0$ m, $D = 21°$, $2 \le F \le 6$ (5) $\theta = 0°$, $E = 0$ m, $F = 6$, $0° \le D \le 35°$(7)	$\theta = 0°$, $E = 0$ m, $F = 6.0$, $D = 21°$	$\theta = 0°$, $E = 0$ m, $F = 6.0$, $D = 21°$	$\theta = 0°$, $E = 0$ m, $F = 6.0$, $D = 21°$
1.1	$\theta = 0°$, $E = 0$ m, $F = 6.0$, $D = 21°$	$\theta = 0°$, $E = 0$ m, $F = 6.0$, $D = 21°$	$E = 0$ m, $D = 21°$, $F = 6.0$, $-40 \le \theta \le 40°$ (10) $\theta = 0°$, $D = 21°$, $F = 6.0$, $-0.8 \le E \le 0.8$ m (7)	$\theta = 0°$, $E = 0$ m, $D = 21°$, $2 \le F \le 6$ (5) $\theta = 0°$, $E = 0$ m, $F = 6$, $0° \le D \le 35°$(7)	$\theta = 0°$, $E = 0$ m, $F = 6.0$, $D = 21°$	$\theta = 0°$, $E = 0$ m, $F = 6.0$, $D = 21°$	$\theta = 0°$, $E = 0$ m, $F = 6.0$, $D = 21°$
1.3	$\theta = 0°$, $E = 0$ m, $F = 6.0$, $D = 21°$	$\theta = 0°$, $E = 0$ m, $F = 6.0$, $D = 21°$	$E = 0$ m, $D = 21°$, $F = 6.0$, $-40 \le \theta \le 40°$ (10) $\theta = 0°$, $D = 21°$, $F = 6.0$, $-0.8 \le E \le 0.8$ m (7)	$\theta = 0°$, $E = 0$ m, $D = 21°$, $2 \le F \le 6$ (5) $\theta = 0°$, $E = 0$ m, $F = 6$, $0° \le D \le 35°$(7)	$\theta = 0°$, $E = 0$ m, $2 \le F \le 6$, $0° \le D \le 35°$ (35)	$\theta = 0°$, $E = 0$ m, $F = 6.0$, $D = 21°$	$\theta = 0°$, $E = 0$ m, $F = 6.0$, $D = 21°$
1.5	$\theta = 0°$, $E = 0$ m, $F = 6.0$, $D = 21°$	$\theta = 0°$, $E = 0$ m, $F = 6.0$, $D = 21°$	$E = 0$ m, $D = 21°$, $F = 6.0$, $-40 \le \theta \le 40°$ (10) $\theta = 0°$, $D = 21°$, $F = 6.0$, $-0.8 \le E \le 0.8$ m (7)	$\theta = 0°$, $E = 0$ m, $D = 21°$, $2 \le F \le 6$ (5) $\theta = 0°$, $E = 0$ m, $F = 6$, $0° \le D \le 35°$(7)	$\theta = 0°$, $E = 0$ m, $F = 6.0$, $D = 21°$	$\theta = 0°$, $E = 0$ m, $F = 6.0$, $D = 21°$	$\theta = 0°$, $E = 0$ m, $F = 6.0$, $D = 21°$
1.7	$\theta = 0°$, $E = 0$ m, $F = 6.0$, $D = 21°$	$\theta = 0°$, $E = 0$ m, $F = 6.0$, $D = 21°$	$E = 0$ m, $D = 21°$, $F = 6.0$, $-40 \le \theta \le 40°$ (10) $\theta = 0°$, $D = 21°$, $F = 6.0$, $-0.8 \le E \le 0.8$ m (7)	$\theta = 0°$, $E = 0$ m, $D = 21°$, $2 \le F \le 6$ (5) $\theta = 0°$, $E = 0$ m, $F = 6$, $0° \le D \le 35°$(7)	$\theta = 0°$, $E = 0$ m, $F = 6.0$, $D = 21°$	$\theta = 0°$, $E = 0$ m, $F = 6.0$, $D = 21°$	$\theta = 0°$, $E = 0$ m, $F = 6.0$, $D = 21°$

APPENDIX A

Scenarios for Rip-Current Simulations

Table A1 provides a summary of the FUNWAVE boundary-condition scenarios used here (Table A1) that also were used in earlier work (Choi et al. 2025). The wave and tide conditions were drawn from observations and then binned into uniformly spaced intervals spanning realistic ranges. Storm-wave cases were not included, both because such conditions approach known modeling limitations and because swimmer exposure usually is negligible during these events. Accordingly, the scenario selection emphasizes low- to moderate-energetic conditions under which rip currents can pose less obvious, yet consequential, hazards to beach users.

APPENDIX B

Locations of Maximum Rip-Current Speed for the 2 October Duck Simulations

For each 1-h simulation (210 cases using the 2 October bathymetry at Duck), the location of the maximum offshore-directed current (averaged over two wave periods) was identified (Fig. B1). Overall, the maximum offshore-directed flow speeds occur predominantly within the surfzone, and many are concentrated near rip channels. This spatial distribution suggests that restricting the velocity extraction to a nearshore "swim zone" (i.e., within a few hundred meters of the shoreline) unlikely would alter substantially the representative maximum-speed metric used here.

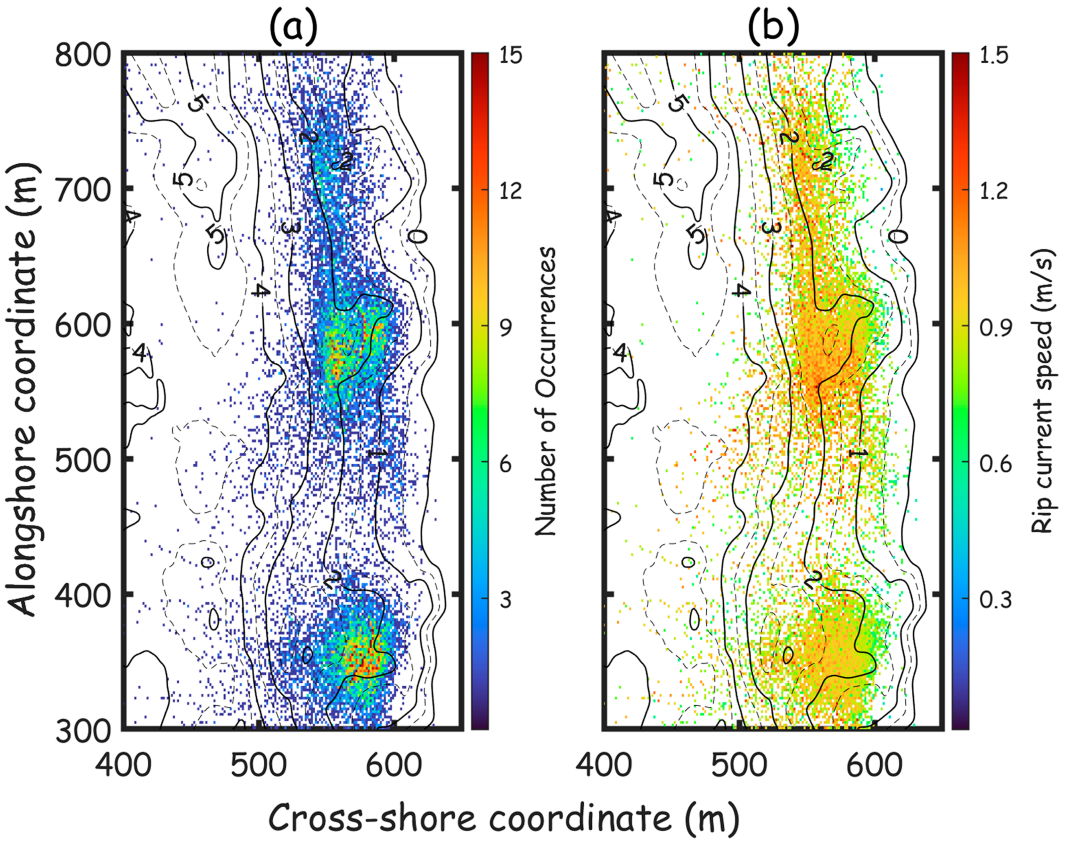

FIG. B1. (a) Number of maximum rip currents (color scale on the right; red is ~15 occurrences at that location) and (b) maximum rip-current velocity averaged over the occurrences (color scale on the right) as functions of cross-shore and alongshore coordinates for simulations using the 2 Oct bathymetry at Duck. Locations were identified from currents averaged over two wave periods within each time window for 1-h simulations across 210 cases. Bathymetric contour curves are drawn every 1 m.

However, the locations of the peak offshore-directed flows can vary and not always are confined to persistent rip channels (Fig. B1), especially during short-crested, multidirectional random waves that can produce transient and spatially intermittent rip currents (Peregrine 1998, 1999; Brocchini et al. 2004; Johnson and Pattiaratchi 2006; Kennedy et al. 2006; Feddersen 2014; Nuss et al. 2025). Thus, predicting the exact rip-current position at any given time remains challenging even within the same beach area.

APPENDIX C

Statistical Assessments of the Rip-Current Prediction

a. Validation statistics

The Brier skill score (BSS) was used to evaluate the forecast skill of the prediction model relative to climatology. BSS is derived from the Brier score (BS), which measures the mean squared error between predicted probabilities and observed binary outcomes (Wilks 2006):

$$\mathrm{BS} = \frac{1}{N}\sum_{i=1}^{N}(p_i - o_i)^2. \tag{C1}$$

Here, N is the total number of forecasts, p_i denotes the predicted probability (0–1), and o_i is the observed outcome (1 for occurrence, 0 otherwise). Observed outcomes were defined by whether rip-current velocity exceeded specified thresholds. Because the threshold velocity defining hazardous conditions is uncertain, BSS was computed across a range of values (u_{th} = 0.35–1.05 m s^{-1}) to assess sensitivity to this choice. The reference Brier score ($\mathrm{BS}_{\mathrm{ref}}$), based on climatology, is defined as

$$\mathrm{BS}_{\mathrm{ref}} = \bar{o}(1 - \bar{o}), \tag{C2}$$

where $\bar{o}$ is the climatological event frequency, i.e., the long-term average probability of occurrence across the dataset. Finally, BSS is expressed as

$$\mathrm{BSS} = 1 - \mathrm{BS}/\mathrm{BS}_{\mathrm{ref}}. \tag{C3}$$

A BSS close to 1 indicates excellent predictive skill relative to climatology, whereas values near or below 0 indicate little or no improvement.

Model performance was further evaluated using categorical metrics derived from a confusion matrix. Model predictions of rip-current occurrence were defined as cases where

the predicted likelihood exceeded a critical threshold (RL_{cr}). These predictions were then compared with observed occurrences, which were treated as binary outcomes. Accuracy (ACC), representing the proportion of correct predictions, was calculated as

$$\mathrm{ACC} = \frac{\mathrm{TP} + \mathrm{TN}}{\mathrm{TP} + \mathrm{FP} + \mathrm{FN} + \mathrm{TN}}, \tag{C4}$$

where true positive (TP) and true negative (TN) indicate correct predictions and false positive (FP) and false negative (FN) represent incorrect predictions. Additional metrics included the probability of detection (POD) and the false alarm ratio (FAR), calculated, respectively, as

$$\mathrm{POD} = \mathrm{TPR} = \frac{\mathrm{TP}}{\mathrm{TP} + \mathrm{FN}}, \tag{C5}$$

$$\mathrm{FAR} = \frac{\mathrm{FP}}{\mathrm{TP} + \mathrm{FP}}. \tag{C6}$$

The TP rate (TPR), identical to POD, measures the sensitivity of the model, while the FP rate (FPR), reflecting the proportion of false alarms among nonevents, is computed as

$$\mathrm{FPR} = \frac{\mathrm{FP}}{\mathrm{FP} + \mathrm{TN}}. \tag{C7}$$

The optimal probability threshold (i.e., critical rip likelihood, RL_{cr}) for binary classification was determined using Youden's index (Wilks 2006), calculated as

$$\text{Youden index} = \mathrm{TPR} - \mathrm{FPR}. \tag{C8}$$

Additionally, the receiver operating characteristic (ROC) curve, plotting TPR against FPR for varying critical rip likelihood RL_{cr}, was also used. Model performance was quantitatively assessed through the area under the ROC curve (AUC_{ROC}), given by

$$\mathrm{AUC}_{\mathrm{ROC}} = \int_0^1 \mathrm{TPR}\, d(\mathrm{FPR}). \tag{C9}$$

An AUC value approaching 1 indicates excellent predictive capability, whereas an AUC near 0.5 indicates a performance similar to random prediction. Collectively, these metrics provided a comprehensive evaluation of the binary predictive performance of the rip-current prediction model.

b. Statistical assessments

Rip-current prediction performance was first evaluated using a reliability diagram, which compares predicted probabilities (likelihoods) with observed frequencies of hazardous rip speeds (Fig. C1). The observed event frequency was defined as the fraction of cases in which rip-current speeds exceeded specified thresholds. Predicted probabilities and observed frequencies for each threshold speed (u_{th}) were grouped into bins of width 0.1 over the range 0–1. The results indicated that hazardous rip-current speeds rarely occurred at forecast probabilities below 0.3, with such events concentrated at higher probabilities (Fig. C1a). The threshold speed of 0.65 m s^{-1} provided the best correspondence to the ideal 1:1 relationship. At this threshold, the model tended to overpredict events at forecast probabilities below 0.4 and underpredict at probabilities above 0.6. Some of these discrepancies may be attributed to the limited availability of rip-current observations in certain probability ranges. A similar S-shaped pattern was reported previously (Casper et al. 2024). From a warning perspective, the model's tendency to overpredict at lower forecast

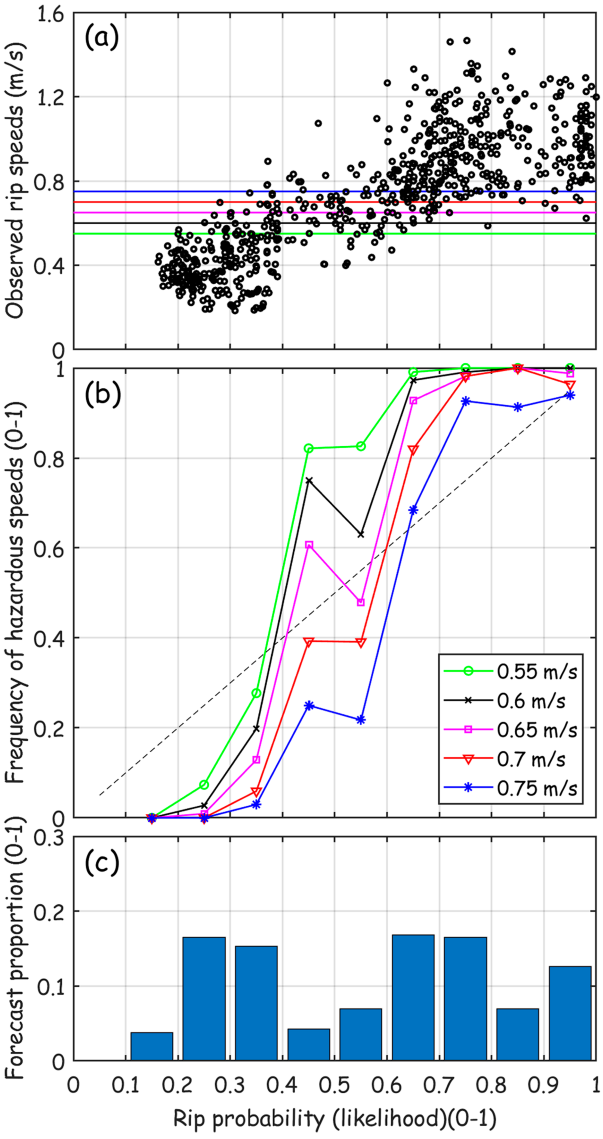

FIG. C1. (a) Observed rip-current speeds, with threshold speeds indicated by horizontal lines [values in the legend of (b)], (b) reliability diagram showing the observed exceedance frequency (symbols connected by colored lines; thresholds in legend), with the dashed line representing perfect reliability (1:1), and (c) refinement distribution showing the relative frequency of predicted likelihood values within each probability bin vs predicted rip-current likelihoods (0–1).

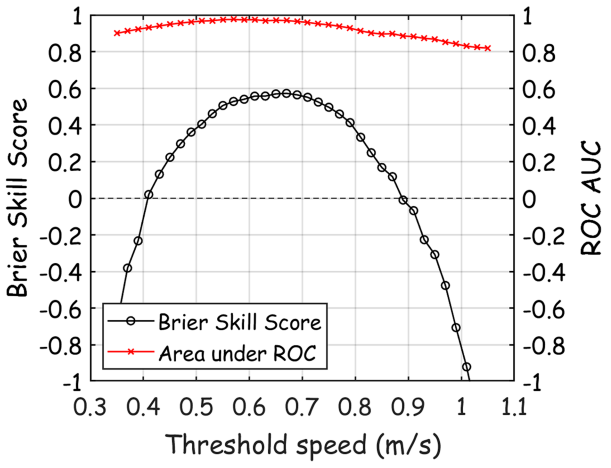

FIG. C2. BSS (black curve; left y axis) and AUC_{ROC} (red curve; right y axis) of the prediction model vs observed rip-current speeds for different threshold speeds. Here, positive BSS values indicate skillful predictions compared with the climatological average, and AUC_{ROC} values approaching 1 indicate excellent predictive capability, while values near 0.5 suggest performance equivalent to random predictions.

likelihoods may be considered beneficial for safety. At higher rip-current speeds, hazardous wave conditions are visually apparent and typically discourage swimming. Thus, underprediction in these high-speed scenarios is unlikely to pose significant safety concerns.

The predictive skill of the rip-current model was evaluated by comparing predicted rip-current occurrences with observations, which were defined as cases where measured rip-current speeds exceeded specified thresholds (Fig. C2). The model demonstrated positive skill (BSS $>$ 0) across threshold speeds ranging from 0.4 to 0.9 m s^{-1}, indicating performance superior to climatological predictions based on average observed conditions. The highest skill (0.5 $<$ BSS $<$ 0.6) was achieved within a relatively broad threshold-speed range (0.55–0.75 m s^{-1}), where model performance was less sensitive to the specific choice of threshold.

Model performance for predicting rip-current occurrences at various threshold speeds and critical likelihoods was assessed using several statistical measures (Table C1). The BSS exceeded 0.5 for threshold speeds between approximately 0.55 and 0.70 m s^{-1} (Fig. C2). Within the 0.55–0.65 m s^{-1} range, model performance metrics derived from the confusion matrix were evaluated across different critical likelihoods. The model demonstrated particularly high predictive capability, with ACC consistently greater than 0.9 for critical likelihoods of 0.4–0.6 (i.e., highlighted by italics in Table C1). In this range, the POD remained high, while the FAR and FPR were generally low, indicating that the model rarely generated unnecessary warnings. For example, at a threshold speed of 0.55 m s^{-1} and a critical likelihood of 0.4, the model achieved an ACC of 0.92, a POD of 0.92, an FAR of 0.03, and an FPR of 0.07. Under these conditions, Youden's index reached 0.85, highlighting this configuration as an optimal balance of rip-current hazard prediction skill. At lower critical likelihoods (e.g., RL_{cr} = 0.3),

TABLE C1. BSS of the prediction model at various threshold speeds u_{th} and corresponding model performance metrics including ACC, FAR, POD, FPR, and Youden's index for different critical likelihood values RL_{cr} used to determine rip-current occurrence predictions. ACC consistently greater than 0.9 for critical likelihoods of 0.4–0.6 is shown in italics.

u_{th} (m s^{-1})	BSS	RL_{cr}	ACC	FAR	TPR (POD)	FPR	Youden's index
0.45	0.22	0.30	0.88	0.10	0.94	0.33	0.61
		0.40	0.86	0.01	0.83	0.03	0.80
		0.50	0.82	0.01	0.78	0.02	0.76
		0.60	0.76	0.00	0.69	0.00	0.69
		0.70	0.59	0.00	0.47	0.00	0.47
0.55	0.51	0.30	0.86	0.17	0.98	0.41	0.57
		0.40	*0.92*	*0.03*	*0.92*	*0.07*	*0.85*
		0.50	*0.90*	*0.02*	*0.87*	*0.04*	*0.83*
		0.60	0.85	0.00	0.78	0.00	0.78
		0.70	0.69	0.00	0.54	0.00	0.54
0.65	0.57	0.30	0.80	0.26	1.00	0.50	0.50
		0.40	*0.91*	*0.11*	*0.96*	*0.17*	*0.79*
		0.50	*0.90*	*0.09*	*0.92*	*0.13*	*0.79*
		0.60	*0.90*	*0.03*	*0.86*	*0.04*	*0.82*
		0.70	0.76	0.01	0.60	0.01	0.59
0.75	0.50	0.30	0.69	0.39	1.00	0.61	0.39
		0.40	0.83	0.26	0.99	0.32	0.67
		0.50	0.85	0.22	0.97	0.26	0.71
		0.60	0.89	0.15	0.94	0.15	0.78
		0.70	0.83	0.07	0.70	0.05	0.65
0.85	0.17	0.30	0.54	0.57	1.00	0.69	0.31
		0.40	0.69	0.47	1.00	0.46	0.53
		0.50	0.73	0.44	0.99	0.40	0.59
		0.60	0.80	0.37	0.98	0.30	0.68
		0.70	0.83	0.27	0.78	0.15	0.63

POD approached unity, but at the cost of higher false alarm rates, reflecting the trade-off between detection and reliability. In addition, model performance was further quantified using the AUC_{ROC}, which yielded a value of 0.97 at the same threshold speed (Fig. C2).

These results suggest that, when applied operationally at Duck, a forecast system issuing warnings based on a critical likelihood of 40% for rip-current speeds above 0.55 m s^{-1} can provide robust hazard prediction performance, supporting its use as a practical decision-making tool.

REFERENCES

Brocchini, M., A. Kennedy, L. Soldini, and A. Mancinelli, 2004: Topographically controlled, breaking-wave-induced macrovortices. Part 1. Widely separated breakwaters. *J. Fluid Mech.*, **507**, 289–307, https://doi.org/10.1017/S002211200400878X.

Casper, A., E. S. Nuss, C. M. Baker, M. Moulton, and G. Dusek, 2024: Assessing NOAA rip-current hazard likelihood predictions: Comparison with lifeguard observations and parameterizations of bathymetric and transient rip-current types. *Wea. Forecasting*, **39**, 1045–1063, https://doi.org/10.1175/WAF-D-23-0181.1.

Castelle, B., R. J. McCarroll, R. W. Brander, T. Scott, and B. Dubarbier, 2016a: Modelling the alongshore variability of optimum rip current escape strategies on a multiple rip-channelled beach. *Nat. Hazards*, **81**, 663–686, https://doi.org/10.1007/s11069-015-2101-3.

——, T. Scott, R. W. Brander, and R. J. McCarroll, 2016b: Rip current types, circulation and hazard. *Earth. Sci. Rev.*, **163**, 1–21, https://doi.org/10.1016/j.earscirev.2016.09.008.

——, J. Dehez, J.-P. Savy, S. Liquet, and D. Carayon, 2025: Semi-empirical forecast modelling of rip-current and shore-break wave hazards. *Nat. Hazards Earth Syst. Sci.*, **25**, 2379–2397, https://doi.org/10.5194/nhess-25-2379-2025.

Chen, Q., R. A. Dalrymple, J. T. Kirby, A. B. Kennedy, and M. C. Haller, 1999: Boussinesq modeling of a rip current system. *J. Geophys. Res.*, **104**, 20 617–20 637, https://doi.org/10.1029/1999JC900154.

——, J. T. Kirby, R. A. Dalrymple, A. Kennedy, and A. Chawla, 2000: Boussinesq modeling of wave transformation, breaking, and runup. II: 2D. *J. Waterway, Port, Coastal, Ocean Eng.*, **126**, 48–56, https://doi.org/10.1061/(ASCE)0733-950X(2000)126:1(48).

——, ——, ——, F. Shi, and E. B. Thornton, 2003: Boussinesq modeling of longshore currents. *J. Geophys. Res.*, **108**, 3362, https://doi.org/10.1029/2002JC001308.

Choi, J., 2022: A modification of the rip current warning system utilizing real-time observations: A database function of likelihood distributions. *J. Korea Water Resour. Assoc.*, **55**, 843–854, https://doi.org/10.3741/JKWRA.2022.55.10.843.

——, 2023: Application of rip current likelihood distributions on rip current forecast system. *J. Korea Water Resour. Assoc.*, **56**, 521–528, https://doi.org/10.3741/JKWRA.2023.56.8.521.

——, 2025: A rip-current prediction/forecast model employing likelihoods of rip currents beforehand simulated by a phase-resolving wave-current model. *Ocean Eng.*, **331**, 121153, https://doi.org/10.1016/j.oceaneng.2025.121153.

——, J. T. Kirby, and S. B. Yoon, 2015: Boussinesq modeling of longshore currents in the SandyDuck experiment under directional random wave conditions. *Coastal Eng.*, **101**, 17–34, https://doi.org/10.1016/j.coastaleng.2015.04.005.

——, S. Elgar, and J. T. Kirby, 2025: Rip current likelihood as a function of incident wave conditions for different bathymetries. *Appl. Ocean Res.*, **162**, 104727, https://doi.org/10.1016/j.apor.2025.104727.

Churma, M. E., and Coauthors, 2017: Observation methodologies for NOAA operational rip current forecast models. *15th Symp. on the Coastal Environment*, Seattle, WA, Amer. Meteor. Soc., 2.3, https://ams.confex.com/ams/97Annual/webprogram/Paper315894.html.

Clark, D. B., S. Elgar, and B. Raubenheimer, 2012: Vorticity generation by short-crested wave breaking. *Geophys. Res. Lett.*, **39**, L24604, https://doi.org/10.1029/2012GL054034.

Dalrymple, R. A., J. H. MacMahan, A. J. H. M. Reniers, and V. Nelko, 2011: Rip currents. *Annu. Rev. Fluid Mech.*, **43**, 551–581, https://doi.org/10.1146/annurev-fluid-122109-160733.

Dusek, G., and H. Seim, 2013a: Rip current intensity estimates from lifeguard observations. *J. Coastal Res.*, **288**, 505–518, https://doi.org/10.2112/JCOASTRES-D-12-00117.1.

——, and ——, 2013b: A probabilistic rip current forecast model. *J. Coastal Res.*, **289**, 909–925, https://doi.org/10.2112/JCOASTRES-D-12-00118.1.

——, A. Van der Westhuysen, A. Gibbs, D. King, S. Kennedy, H. Seim, and D. Elder, 2014: Coupling a rip current forecast model to the nearshore wave prediction system. *12th Symp. on the Coastal Environment*, Atlanta, GA, Amer. Meteor. Soc., 3.2, https://ams.confex.com/ams/94Annual/webprogram/Manuscript/Paper238859/Dusek%20et%20al.%20-%20Coupling%20rip%20current%20forecast%20model%20to%20NWPS.pdf.

Elgar, S., and B. Raubenheimer, 2020: Field evidence of inverse energy cascades in the surfzone. *J. Phys. Oceanogr.*, **50**, 2315–2321, https://doi.org/10.1175/JPO-D-19-0327.1.

——, C. Dooley, L. Gorrell, and B. Raubenheimer, 2023: Observations of two-dimensional turbulence in the surfzone. *Phys. Fluids*, **35**, 085142, https://doi.org/10.1063/5.0159170.

Engle, J. A., 2003: Formulation of a rip current forecasting technique through statistical analysis of rip current-related rescues. M.S. thesis, Dept. of Civil and Coastal Engineering, University of Florida, 81 pp.

Feddersen, F., 2014: The generation of surfzone eddies in a strong alongshore current. *J. Phys. Oceanogr.*, **44**, 600–617, https://doi.org/10.1175/JPO-D-13-051.1.

Geiman, J. D., and J. T. Kirby, 2013: Unforced oscillation of rip-current vortex cells. *J. Phys. Oceanogr.*, **43**, 477–497, https://doi.org/10.1175/JPO-D-11-0164.1.

Gensini, V. A., and W. S. Ashley, 2010: An examination of rip current fatalities in the United States. *Nat. Hazards*, **54**, 159–175, https://doi.org/10.1007/s11069-009-9458-0.

Goda, Y., 1970: Numerical experiments on wave statistics with spectral simulation. Rep of the Port and Harbour Research Institute 8, 56 pp.

HR Wallingford, 2005: R&D outputs: Flood risks to people. The Risks to People Methodology Phase 2, FD2321/TR1, 103 pp.

Johnson, D., and C. Pattiaratchi, 2006: Boussinesq modelling of transient rip currents. *Coastal Eng.*, **53**, 419–439, https://doi.org/10.1016/j.coastaleng.2005.11.005.

Kennedy, A. B., Q. Chen, J. T. Kirby, and R. A. Dalrymple, 2000: Boussinesq modeling of wave transformation, breaking, and runup. I: 1D. *J. Waterway, Port, Coastal, Ocean Eng.*, **126**, 39–47, https://doi.org/10.1061/(ASCE)0733-950X(2000)126:1(39).

——, M. Brocchini, L. Soldini, and E. Gutierrez, 2006: Topographically controlled, breaking-wave-induced macrovortices.

Part 2. Changing geometries. *J. Fluid Mech.*, **559**, 57–80, https://doi.org/10.1017/S0022112006009979.

Kirby, J. T., and H. T. Özkan, 1994: Combined refraction diffraction model for spectral wave conditions, REF DIFS, version 1.1: Documentation and user's manual. CACR Rep. No. 94 04, Center for Applied Coastal Research, Dept. of Civil Engineering, University of Delaware.

Lascody, R. L., 1998: East central Florida rip current program. *Natl. Wea. Dig.*, **22**, 25–30.

Liu, Y., 2020: Rip currents in Lake Michigan and in Lake Superior. Ph.D. dissertation, The University of Wisconsin–Madison, 209 pp.

——, and C. H. Wu, 2022: Rip currents near coastal structures in Lake Michigan: Characterization and assessment for warnings. *J. Great Lakes Res.*, **48**, 645–658, https://doi.org/10.1016/j.jglr.2022.03.001.

Longuet-Higgins, M. S., D. E. Cartwright, and N. D. Smith, 1963: Observations of the directional spectrum of sea waves using the motions of a floating buoy. *Ocean Wave Spectra*, Prentice-Hall, 111–136.

Lushine, J., 1991: A study of rip current drownings and related weather factors. *Natl. Wea. Dig.*, **16**, 13–19.

MathWorks, 2024: *trainbr*: Bayesian regularization backpropagation. MathWorks, accessed 18 August 2025, https://www.mathworks.com/help/deeplearning/ref/trainbr.html.

McCarroll, R. J., B. Castelle, R. W. Brander, and T. Scott, 2015: Modelling rip current flow and bather escape strategies across a transverse bar and rip channel morphology. *Geomorphology*, **246**, 502–518, https://doi.org/10.1016/j.geomorph.2015.06.041.

Mitsuyasu, H., F. Tasai, T. Suhara, S. Mizuno, M. Ohkusu, T. Honda, and K. Rikiishi, 1975: Observations of the directional spectrum of ocean WavesUsing a cloverleaf buoy. *J. Phys. Oceanogr.*, **5**, 750–760, https://doi.org/10.1175/1520-0485(1975)005<0750:OOTDSO>2.0.CO;2.

Moulton, M., G. Dusek, S. Elgar, and B. Raubenheimer, 2017: Comparison of rip current hazard likelihood forecasts with observed rip current speeds. *Wea. Forecasting*, **32**, 1659–1666, https://doi.org/10.1175/WAF-D-17-0076.1.

——, S. H. Suanda, J. C. Garwood, N. Kumar, M. R. Fewings, and J. M. Pringle, 2023: Exchange of plankton, pollutants, and particles across the nearshore region. *Ann. Rev. Mar. Sci.*, **15**, 167–202, https://doi.org/10.1146/annurev-marine-032122-115057.

Nelko, V., and R. A. Dalrymple, 2008: Rip currents: Mechanisms and observations. *Proceeding of 31st International Conference Coastal Engineering*, J. M. Smith, Ed., World Scientific, 888–900.

NOAA, 2022: Weather related fatality and injury statistics. National Weather Service, accessed 15 November 2024, https://weather.gov/hazstat/.

Nuss, E. S., M. Moulton, S. H. Suanda, and C. M. Baker, 2025: Modeled surf-zone eddies on a laboratory scale barred beach with varying wave conditions. *J. Geophys. Res. Oceans*, **130**, e2023JC020549, https://doi.org/10.1029/2023JC020549.

Peregrine, D. H., 1998: Surf zone currents. *Theor. Comput. Fluid Dyn.*, **10**, 295–309, https://doi.org/10.1007/s001620050065.

——, 1999: Large-scale vorticity generation by breakers in shallow and deep water. *Eur. J. Mech.*, **18B**, 403–408, https://doi.org/10.1016/S0997-7546(99)80037-5.

RESCDAM, 2000: The use of physical models in dam-break flood analysis. Final Report of Helsinki University of Technology data, December 2000. Appendix 2 to Final Report of RESCDAM, June 2001, 48 pp.

Salatin, R., Q. Chen, A. S. Bak, F. Shi, and S. R. Brandt, 2021: Effects of wave coherence on longshore variability of nearshore wave processes. *J. Geophys. Res. Oceans*, **126**, e2021JC017641, https://doi.org/10.1029/2021JC017641.

Schrader, M., 2004: Evaluation of the modified ECFL LURCS rip current forecasting scale and conditions of selected rip current events in Florida. M.S. thesis, Dept. of Civil and Coastal Engineering, University of Florida, 89 pp.

Spydell, M., and F. Feddersen, 2009: Lagrangian drifter dispersion in the surf zone: Directionally spread, normally incident waves. *J. Phys. Oceanogr.*, **39**, 809–830, https://doi.org/10.1175/2008jpo3892.1.

Suanda, S. H., and F. Feddersen, 2015: A self-similar scaling for cross-shelf exchange driven by transient rip currents. *Geophys. Res. Lett.*, **42**, 5427–5434, https://doi.org/10.1002/2015gl063944.

Surf Life Saving, 2022: National Coastal Safety Report 2022. https://issuu.com/surflifesavingaustralia/docs/ncsr_2022.

Tang, E.-S., and R. A. Dalrymple, 1989: Nearshore circulation: rip currents and wave groups. *Advances in Coastal and Ocean Engineering*, Plenum Press, 205–230.

Tipton, M., T. Reilly, A. Rees, G. Spray, and F. Golden, 2008: Swimming performance in surf: The influence of experience. *Int. J. Sports Med.*, **29**, 895–898, https://doi.org/10.1055/s-2008-1038510.

Wei, G., J. Kirby, S. T. Grilli, and R. Subraymanya, 1995: A fully nonlinear Boussinesq model for surface waves. Part 1. Highly nonlinear unsteady waves. *J. Fluid Mech.*, **294**, 71–92, https://doi.org/10.1017/S0022112095002813.

Wilks, D. S., 2006: *Statistical Methods in the Atmospheric Sciences.* 2nd ed. International Geophysics Series, Vol. 91, Academic Press, 649 pp.

Yuan, Y., H. Yang, F. Yu, Y. Gao, B. Li, and C. Xing, 2023: A wave-resolving modeling study of rip current variability, rip hazard, and swimmer escape strategies on an embayed beach. *Nat. Hazards Earth Syst. Sci.*, **23**, 3487–3507, https://doi.org/10.5194/nhess-23-3487-2023.